Journal of Materials Chemistry A

ROYAL SOCIETY OF CHEMISTRY

PAPER

View Article Online
View Journal | View Issue

Cite this: J. Mater. Chem. A, 2024, 12, 7680

Chemical looping methanol oxidation using supported vanadium phosphorous oxide carriers for formaldehyde production†

Anuj Joshi, ‡[a] Sonu Kumar, ‡[a] Melissa Marx, [b] Amanda H. Trout,[c] Sudeshna Gun,[a] Zain Mohammad,[a] Yehia Khalifa[b] and Liang-Shih Fan *[a]

Received 4th December 2023
Accepted 19th February 2024

DOI: 10.1039/d3ta07468d

rsc.li/materials-a

This work describes the remarkable performance of a novel chemical looping route for the partial oxidation of methanol to formaldehyde employing β-$VOPO_4$ as the oxygen carrier. During reduction, the $VOPO_4$ carrier donates its lattice oxygen to methanol, generating formaldehyde and steam. The reduced carrier, VPO_{5-x}, subsequently replenishes its lattice oxygen by reacting with air during oxidation. This study explores how incorporating $VOPO_4$ on SiO_2 support enables superior lattice oxygen utilization owing to improved active site dispersion. Subsequently, a stable redox performance over 10 redox cycles is achieved for the synthesized carrier. Fixed bed studies showcased a stable methanol conversion of 85% with a corresponding formaldehyde selectivity of 45%. These results confirm the feasibility of $VOPO_4$-based oxygen carrier design for the selective oxidation of methanol to formaldehyde. The insights on carrier development targeted for selective reaction provided in this work can also be leveraged for advancing other chemical looping processes.

1. Introduction

Formaldehyde (HCHO) is an essential organic chemical with industrial significance and has been produced commercially since 1889. It serves as a key feedstock in various products such as resins, paints, polymers, adhesives, and pesticides and is also used in the textile, transport, energy, and personal hygiene industries.[1–6] With the demand for these products rising, formaldehyde production has also witnessed steady growth, with yearly production exceeding 30 megatons.[7,8] Industrially, formaldehyde is produced predominantly from the catalytic oxidation of methanol (CH_3OH), and over 30% of all the methanol produced is dedicated towards its production.[9,10] There are two different processes for producing formaldehyde from methanol, that can be classified based on the catalysts they employ. The first process, the 'silver process,' utilizes a silver-based catalyst. This process involves sending a methanol and air mixture, with methanol in excess over the catalyst bed at ambient pressure and in the temperature range of 600–720 °C.[1] The reaction mechanism entails both the dehydrogenation and partial oxidation of methanol,[11] which are represented in eqn (1) and (2), respectively.

$$CH_3OH \rightarrow HCHO + H_2 \quad (1)$$

$$CH_3OH + \frac{1}{2}O_2 \rightarrow HCHO + H_2O \quad (2)$$

The second process, the 'Formox process,' using an iron-molybdenum catalyst, also operates at ambient pressure but at a considerably lower temperature range of 250–400 °C.[1] Moreover, the process is carried out with an excess air-to-methanol feed ratio and involves only the partial oxidation route (eqn (2)). The yield of both these processes ranges from 86 to 92%.[1,11,12] However, due to its higher selectivity and lower operating temperatures, the Formox process has more market share than the silver process.[13]

Despite the widespread deployment of the two catalytic processes at the industrial scale, certain drawbacks still remain unsolved. The primary concern is the hazard posed by the necessity to make a dangerous mixture of methanol vapors with air at high temperatures.[14] Another drawback is the poor stability of the catalysts. In the case of the silver process, the catalyst undergoes agglomeration due to prolonged operation at high temperatures and needs to be replaced every 3 to 12 months.[14–16] The Formox process with a Fe–Mo catalyst also faces the problem of catalyst deactivation, which can be attributed to the volatilization of MoO_3, formed due to the

[a]William G. Lowrie Department of Chemical and Biomolecular Engineering, The Ohio State University, Columbus, OH 43210, USA. E-mail: fan.1@osu.edu

[b]Department of Chemistry and Biochemistry, The Ohio State University, Columbus, Ohio 43210, USA

[c]Center for Electron Microscopy and Analysis, The Ohio State University, Columbus, OH 43212, USA

† Electronic supplementary information (ESI) available. See DOI: https://doi.org/10.1039/d3ta07468d

‡ These authors have contributed equally to this work and are co-first authors.

reaction of formaldehyde with the catalyst.[17–20] Thus, there has been a significant research thrust in the synthesis of a new catalyst formulation that is low-cost, stable, and sustainable. Oxides of metals such as iron, vanadium, molybdenum, niobium, and phosphates of vanadium, iron, and their mixtures have been researched.[1] Although the results have been promising, a substantial effort to develop an alternative technology altogether has been lacking.

This work introduces a novel chemical looping methanol oxidation (CLMO) process for formaldehyde production. Chemical looping is a system involving redox reactions in two or more steps, facilitated by an oxygen carrier, and has been successfully applied for applications such as syngas and H_2 production.[21–30] Instead of co-feeding air with methanol, in the chemical looping approach, methanol reacts with the lattice oxygen of the carrier to form formaldehyde. The carrier provides the active site as well as the oxygen for executing the reaction. The reduced carrier is subsequently regenerated by reacting with air. This approach completely avoids the contact of methanol and air, thus rendering a safer process than state-of-the-art catalytic technologies. Moreover, significant energy savings can be possibly obtained as excess air is not required to keep the methanol and air mixture below the lower explosive limit.[11,16]

The success of any chemical looping approach depends on its oxygen carrier. Thus, developing an oxygen carrier that is low-cost and recyclable is critical.[24,31–37] Among the various carriers tested for the selective oxidation of hydrocarbon feeds, vanadium phosphorous oxide ($VOPO_4$) is a promising candidate. As mentioned above, some of its phases have been studied as a catalyst for selective methanol oxidation and have exhibited good yields.[38–40] Moreover, vanadium phosphorous oxides have demonstrated their ability to effectively activate C–H bonds in lower alkanes,[41] which can be leveraged in this case. To achieve stability of the oxygen carrier, its active components are often dispersed on a support.[42–46] Our preliminary analysis and literature indicate that SiO_2 can serve as a support for $VOPO_4$ as it does not react with either vanadium or phosphorous and has already been utilized as a carrier support for various applications.[31,47–50] The CLMO process using the VPO carrier can be broken down into two steps. In the first step, $VOPO_4$ (V^{5+} state) reacts with methanol to form formaldehyde, water, and a reduced phase of VPO (VPO_{5-x}) consisting of both V^{4+} and V^{3+} states. The first step can also produce undesired products like CO and CO_2. VPO_{5-x} is then regenerated back into $VOPO_4$ in the subsequent step in the presence of air. The two steps of the process are represented by eqn (3) and (4), and the overall process can be envisioned through the schematic shown in Fig. 1. Moreover, starting with the highest oxidized V^{5+} phase of $VOPO_4$ allows maximum oxygen utilization.

$$VOPO_4 + xCH_3OH \rightarrow xHCHO + VPO_{5-x} \quad (3)$$

$$VPO_{5-x} + \frac{x}{2}O_2 \rightarrow VOPO_4 \quad (4)$$

This work is the first of its kind as it comprehensively establishes a novel chemical looping approach for formaldehyde production using $VOPO_4$ dispersed on SiO_2 support as the carrier through experimental studies. The analysis of the reaction of methanol with $VOPO_4$, along with the effect of multiple redox cycles on the reactivity of the carrier, is studied using thermogravimetric analysis and solid characterization techniques such as X-ray diffraction (XRD), X-ray photoelectron spectroscopy (XPS), Raman spectroscopy, and scanning electron microscopy with energy dispersive spectroscopy (SEM-EDS). Fixed bed experiments in conjunction with transmission electron microscopy (TEM) are conducted to assess the process at a larger scale of operation. The results of this work provide guidelines for developing robust carriers and provide an understanding of underlying chemistry which can be leveraged for enhancing reactivity. Furthermore, this work adds to the few pathways developed for chemical looping selective oxidation apart from syngas and H_2 generation, furthering a broader research thrust in the field.

2. Materials and methods

2.1 VPO carrier synthesis

2.1.1 Synthesis of precursor material. VPO precursor was prepared following the procedure described in previous studies.[51] Stoichiometric amounts ($P:V = 1:1$) of V_2O_5 and H_3PO_4 (85 wt%) were mixed in ethanol and refluxed for 16 hours. 20 ml of ethanol per gram of V_2O_5 was used. After the reflux step, all the ethanol was evaporated. The residue was then collected, crushed, and calcined in air for 10 hours at 500 °C. The obtained yellow powder was labeled as the VPO precursor.

2.1.2 Preparation of supported VPO carrier. VPO samples supported on SiO_2 were prepared in different concentrations, *i.e.*, 0 (unsupported), 30, 50, and 70 wt% SiO_2. The prepared VPO precursor was thoroughly mixed with a pertinent amount of SiO_2 powder and made into a pellet using deionized water. The pellet was then dried overnight at room temperature before being calcined at 550 °C in air for 10 hours. The prepared redox carriers were labeled as VPO-Un, VPO-30Si, VPO-50Si, and VPO-70Si.

2.2 Solid characterization

A Quantachrome NOVA 4200e analyzer was used to estimate the surface area of the prepared carriers through the Brunauer–Emmett–Teller (BET) method. Degassing of samples was done overnight at 300 °C and under vacuum to remove any adsorbed species. Subsequently, the samples underwent isothermal nitrogen adsorption at a temperature of −196 °C for their surface area determination.

The laser Raman spectra were collected in a Renishaw IR Microprobe at room temperature. All measurements were performed using a 514 nm laser and a 10× objective lens with a grating of 1200 lines per mm. The spectra were collected at an exposure time of 10 seconds and averaged over 2 scans to improve the signal-to-noise ratio.

The crystalline phases of the fresh and post-experiment samples were identified through X-ray diffraction (XRD) analysis which was conducted in a Rigaku SmartLab X-ray

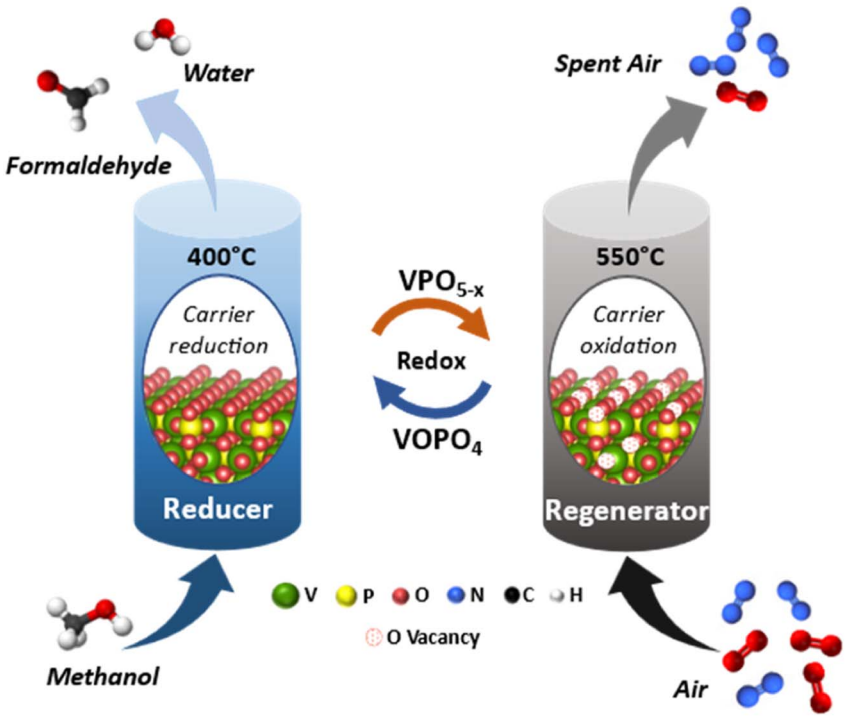

Fig. 1 Simplified process schematic of CLMO.

Diffractometer fitted with a diffraction beam monochromator. An accelerating voltage of 40 kV with a filament current of 44 mA was used to acquire the scans from 15 to 65° at a scanning rate of 2° min^{-1}. The ICDD database in the PDXL2 software was used to identify the phases in the XRD spectra.

For the X-ray Photoelectron Spectroscopy (XPS) analysis, all samples were collected on the NEXSA G1 (Thermo Scientific) with an Al Kα source (1486.6 eV). Survey spectrum was collected for all samples (pass energy 150, step size 1.0 eV, and dwell time 10 ms). High resolution spectra for C 1s, O 1s, P 2p, V 2p, and Si 2s were collected at pass energy 40, step size 0.1 eV, dwell time 100 ms. All spectra were calibrated to the aliphatic carbon feature (284.5 eV). Casa XPS software (version 2.3.25) was used for the data analysis with either Shirley or linear background subtraction. Non-metal peaks were fit with GL(30), and metal peaks were fit with GL(70), respectively.

A Thermo Scientific Apreo 2 Scanning Electron Microscope (SEM) was used to acquire high resolution images for investigating carriers' surface morphology. The images were acquired with a 5 kV and 50 pA electron beam at a working distance of 3.2 mm. Additionally, to ascertain the elemental distribution on the surface of the carriers, energy dispersive X-ray spectroscopy (EDS) mapping was performed at 30 kV with a 1.6 nA electron beam.

All TEM images were collected on an FEI Tecnai F20 TEM operating at 200 kV. The high-resolution TEM images were collected with a 40-micron objective aperture.

2.3 Thermogravimetric analysis

All the thermogravimetric analyses were carried out in a Setaram SETSYS Evolution Thermogravimetric analyzer (TGA). To examine the phase evolution of the VPO carrier, VPO-Un sample with a loading of ~30 mg was subjected to reduction for 3 hours, 6 hours, and 12 hours. During reduction, a stream of 100 ml min^{-1} CH_3OH (1010 ppm, balance N_2) was injected at 400 °C for the respective time duration. Moreover, for establishing the carrier's phase regenerability, the 3 hours reduced sample was oxidized after reduction, wherein 100 ml min^{-1} of air along with 100 ml min^{-1} N_2 at 550 °C was injected for 180 min. During the experiment, 100 ml min^{-1} N_2 was sent as a flushing gas for 5 minutes before and after the reduction and oxidation steps. A flushing of 100 ml min^{-1} N_2 was used during the temperature transition between the reduction and oxidation steps.

Methanol temperature programmed reduction (CH_3OH-TPR) experiments were carried out to examine the effect of support's concentration on the VPO carriers. Prior to TPR, the samples were first activated by subjecting them to 1 CH_3OH-Air redox cycle. To carry out the redox cycle, the carriers were first reduced, wherein 100 ml min^{-1} CH_3OH (1010 ppm, balance N_2) was introduced at 400 °C for 30 min, followed by their regeneration, wherein 100 ml min^{-1} of air with 100 ml min^{-1} N_2 at 550 °C was injected for 20 min. Post this activation step, the TGA with the oxidized sample was cooled down to 200 °C under a flow of 100 ml min^{-1} N_2. To ensure the temperature of the TGA is stabilized, the sample was maintained at 200 °C for 15 min under 100 ml min^{-1} of N_2. The temperature was then increased from 200 °C to 550 °C at the rate of 5°C min^{-1} under 100 ml min^{-1} CH_3OH (1010 ppmv, balance N_2). eqn (5) was used to calculate the time derivative of weight (dTg), which was plotted against temperature to obtain the TPR profiles.

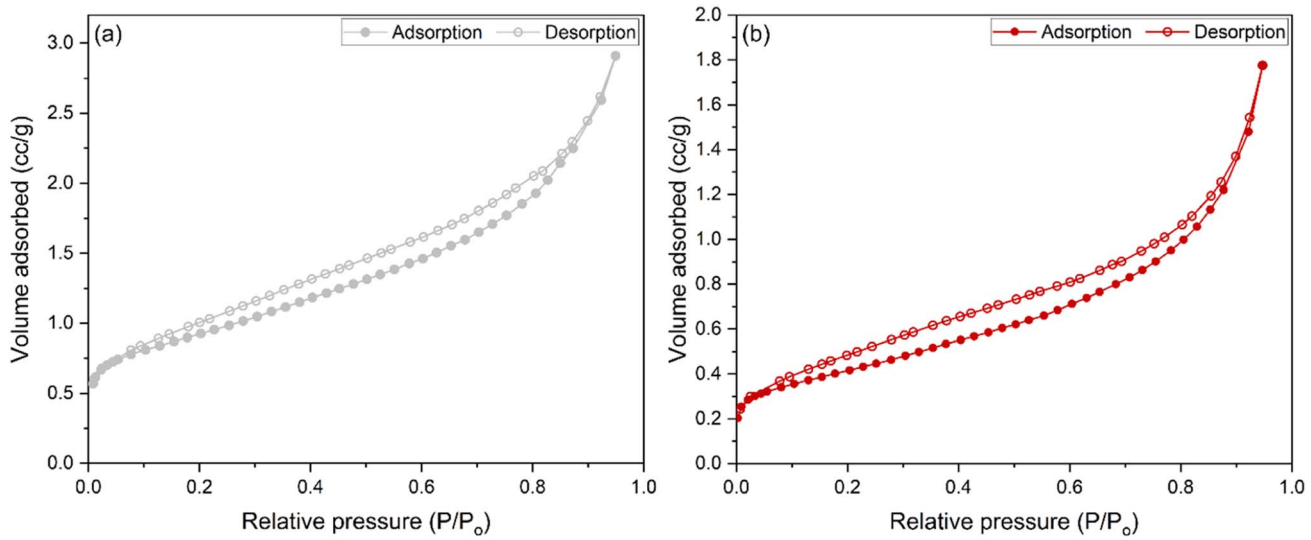

Fig. 2 N_2 adsorption–desorption isotherms for fresh (a) VPO-Un and (b) VPO-70Si carriers.

$$\mathrm{dTg} = \frac{W_2 - W_1}{t_2 - t_1} \quad (5)$$

(W_1 and W_2 are the weight of samples at times t_1 and t_2, respectively).

To test the recyclability and stability, the prepared VPO carriers were put through 10 continuous CH_3OH-air redox cycles. For every redox cycle, the sample first underwent reduction, wherein 100 ml min^{-1} CH_3OH (1010 ppm, balance N_2) was introduced at 400 °C for 30 min, which was followed by regeneration, wherein 100 ml min^{-1} of air with 100 ml min^{-1} N_2 was injected at 550 °C for 20 min. During the experiment, 100 ml min^{-1} N_2 was sent as a flushing gas for 5 minutes before and after the reduction and oxidation steps. A flushing of 100 ml min^{-1} N_2 was also used during temperature transitions between the reduction and oxidation steps. To minimize the variability due to sample loading in the TGA, the weight of the sample prior to every experiment was kept in the range of 25–30 mg on the TGA crucible. Using the obtained weight data, the reduction of the carrier for each cycle was calculated as the oxygen weight loss per weight of the VPO (active component) in the loaded carrier, as per eqn (6).

$$\text{Oxygen loss or reduction} = \frac{\Delta W}{M_i \times x_i} \quad (6)$$

(ΔW is the net weight change observed for a reduction step, M_i is the weight of the sample at the start of the experiment, and x_i is the mass fraction of VPO in the carrier).

During all TGA experiments, a constant flow of 50 ml min^{-1} He was maintained as a protective gas.

2.4 Fixed bed analysis

The CH_3OH reduction step was studied at 400 °C in a fixed bed setup for the VPO-Un and VPO-70Si carriers, as depicted in Fig. S1.† For the reactor, a ceramic tube of 0.5-inch ID was utilized, and 0.1 g of sample was loaded. During reduction, 1010 ppmv CH_3OH gas (balanced with N_2) was injected at a flow rate of 15 ml min^{-1} in the reactor. A post reactor dilution stream of 185 ml min^{-1} of N_2 was maintained. The reduction was carried out for 333 minutes for the VPO-Un carrier and 100 minutes for VPO-70Si carrier to keep the total amount of reactant gas inlet per unit active component the same across all experiments. Continuous gas monitoring was done at the reactor outlet using a CAI 6000 FT-IR gas analyzer. The reduced carrier was oxidized at 550 °C using 100 ml min^{-1} of air for 60 minutes. Using the data obtained, % CH_3OH conversion and % HCHO selectivity were calculated using eqn (7) and (8), respectively, and plotted against time.

$$CH_3OH\ \text{conversion}(\%) = \frac{CH_3OH_{in} - CH_3OH_{out}}{CH_3OH_{in}} \times 100 \quad (7)$$

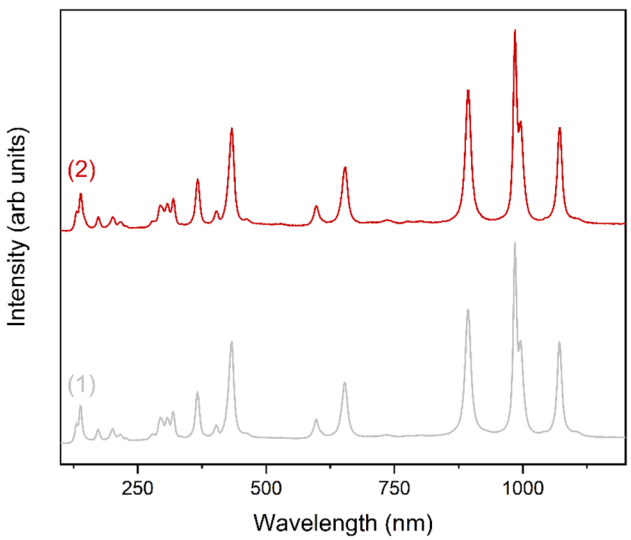

Fig. 3 Raman spectra of fresh (1) VPO-Un and (2) VPO-70Si carriers.

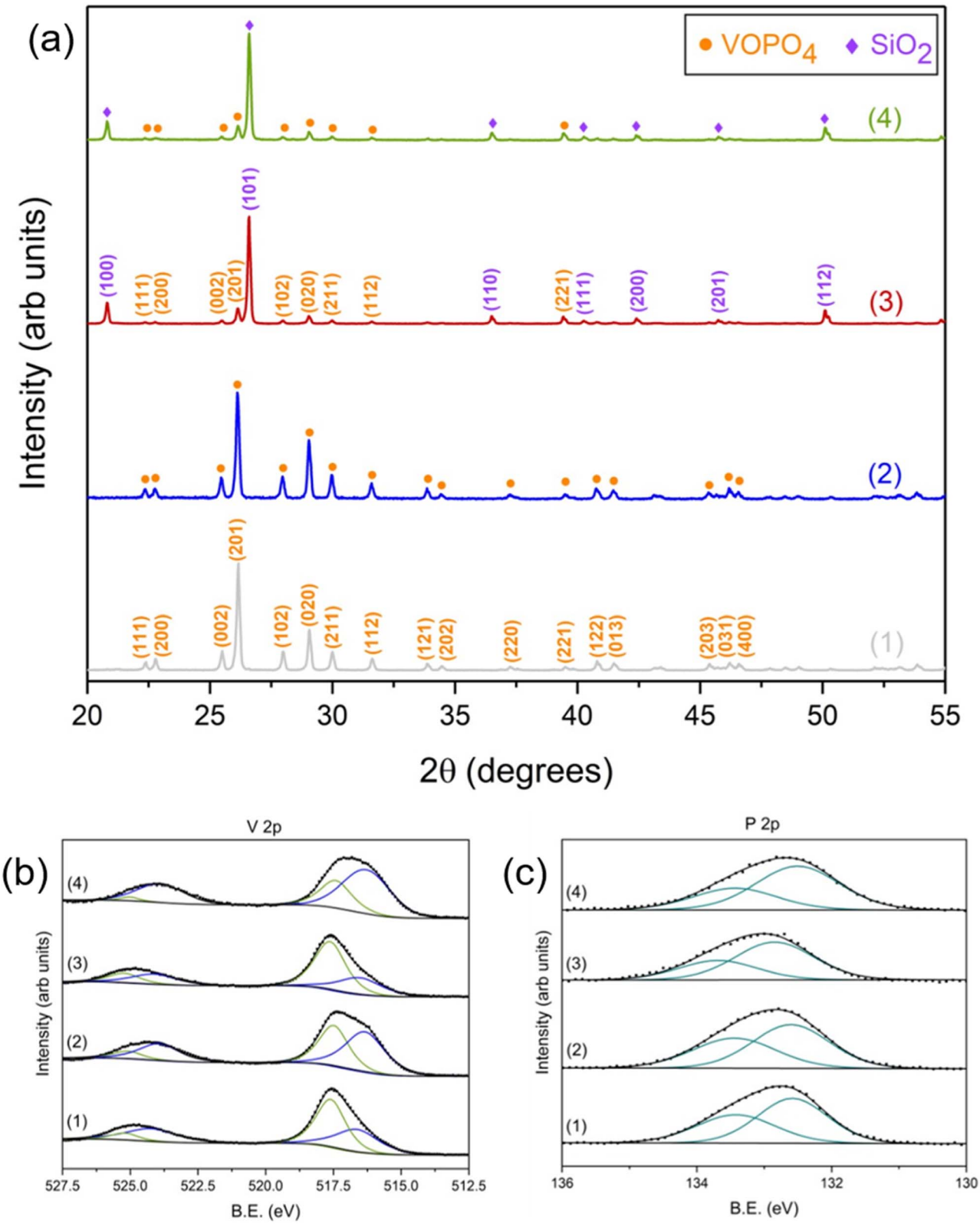

Fig. 4 (a) XRD spectra (b) V 2p XPS spectra and (c) P 2p XPS spectra of VPO-Un (1) before and (2) after 10 redox cycles and of VPO-70Si (3) before and (4) after 10 redox cycles.

(CH_3OH_{in} and CH_3OH_{out} are the concentration of methanol at the inlet and the outlet at time t, respectively).

$$\text{HCHO selectivity} = \frac{\text{HCHO}_{out}}{\text{HCHO}_{out} + \text{CO}_{2out} + \text{CO}_{out} + \text{C}_{dep}} \times 100 \quad (8)$$

($HCHO_{out}$, CO_{2out} and CO_{out} are the concentration of CO_2 and CO at the outlet at time t, respectively).

C_{dep} in eqn (8) is the instantaneous molar rate of carbon deposition and is calculated using eqn (9).

$$C_{dep}\ (\text{ppm min}^{-1}) = CH_3OH_{in} - (CH_3OH_{out} + HCHO_{out} + CO_{2out} + CO_{out}) \quad (9)$$

It is important to note that the total outlet flow rate was assumed to be identical to the total inlet flow rate allowing for the above calculations (eqn (7)–(9)). The basis of this assumption is the low CH_3OH flow rate compared to the diluent N_2.

3. Results and discussion

3.1 Characterization of the VPO carrier

3.1.1 Isothermal N_2 physisorption. In order to determine the surface area of the fresh VPO carriers, N_2 adsorption–desorption isotherms analysis was conducted, the findings of which are presented in Fig. 2. The isotherms can be classified as type II, indicating a non-porous or macroporous structure.[52] The surface area of VPO-Un and VPO-70Si carriers were determined as 0.82 $m^2\ g^{-1}$ and 1.12 $m^2\ g^{-1}$, respectively. This increase may be attributed to the improved dispersion of VPO on the support, which could enhance reactivity. For comparison, the surface area of calcined SiO_2 (which contains 0% active material) was found to be 1.088 $m^2\ g^{-1}$, a value notably similar to that of the VPO-70Si carrier. Additionally, the N_2 adsorption–desorption isotherms for calcined SiO_2 is depicted in Fig. S2.†

3.1.2 Solid characterization. The Raman spectrum for the VPO-Un and the VPO-70Si fresh carriers is depicted in Fig. 3(1) and (2), respectively. Both spectra have four characteristic peaks at 893 cm^{-1}, 985 cm^{-1}, 995 cm^{-1}, and 1071 cm^{-1} which indicate the presence of the β-$VOPO_4$ phase.[53–55] Furthermore, no impurity phase formation is occurring due to the SiO_2 support, as the spectrum for both the carriers is identical.

The XRD analysis of the fresh VPO-Un and VPO-70Si, shown in Fig. 4(a), reveals the presence of β-$VOPO_4$ (ICDD – 01-084-9976) and SiO_2 (ICDD – 00-046-1045). This validates that the synthesis of the carriers was successful, and the SiO_2 support does not react with $VOPO_4$. Moreover, both carriers maintained their phase integrity as no presence of any additional phases were detected after 10 redox cycles, as depicted in Fig. 4(a). Thus, both the carriers are able to sustain phase stability and integrity over multiple cycles, which involve exposure to CH_3OH and air along with temperature swing. The intermediate SiO_2 concentration carriers, VPO-30Si and VPO-50Si, were also synthesized successfully and maintained their phase integrity over 10 redox cycles. Their XRD analysis is presented in Fig. S3.†

XPS spectra were also collected on the VPO-Un and VPO-70Si fresh and post redox carriers to understand any surface modifications or changes to the oxidation states. V 2p spectra, represented in Fig. 4(b), indicate the presence of two sets of doublets (V $2p_{3/2}$ and V $2p_{1/2}$) that are representative of both the V^{5+} (517.6 eV and 525.2 eV) and the V^{4+} state. (516.6 eV and 524.2 eV).[56–64] However, after both carriers undergo redox cycling, the ratio of V^{4+} to V^{5+} on the surface increases. This can be attributed to higher oxygen vacancies present on the surface after 10 redox cycles. Fig. 4(c) shows the complementary P 2p XPS spectra of the same samples. For the VPO-Un carrier, the binding energies of the features appear at 132.6 eV and 133.4 eV representing the P $2p_{3/2}$ and P $2p_{1/2}$, respectively. They do not shift as a function of cycling, suggesting that P is not changing

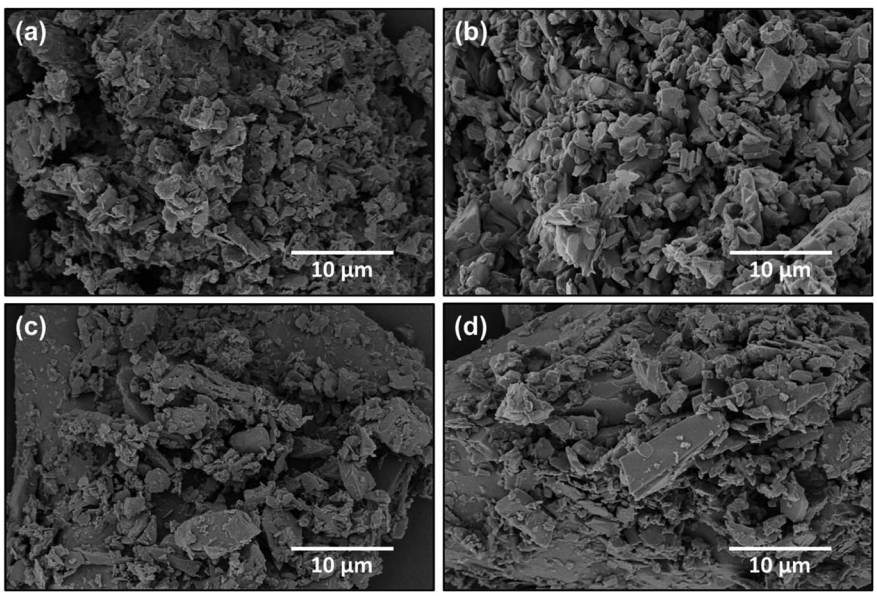

Fig. 5 SEM image of VPO-Un (a) before and (b) after 10 redox cycles and of VPO-70Si (c) before and (d) after 10 redox cycles.

oxidation states on the surface of the material. For the VPO-70Si carrier, the P $2p_{3/2}$ and P $2p_{1/2}$ appear at 132.7 eV and 133.6 eV, which is within a reasonable binding energy shift of the unsupported carrier and does not vary as a function of redox cycling. The XPS analysis for other elements for the fresh and post redox carriers is provided in ESI (Section S4).† Furthermore, XPS analysis on VPO-Un and VPO-70Si carriers after 1 redox cycle, representing the activation cycle, is also given in the ESI (Section S5).†

The fresh and post-redox VPO-Un and 70-Si carriers were also subjected to SEM and EDS analysis to assess their morphological evolution. SEM imaging, shown in Fig. 5, revealed a wide distribution in crystal sizes for $VOPO_4$ for both the fresh carriers. Furthermore, $VOPO_4$ was observed to be well dispersed on the SiO_2 support for the VPO-70Si carrier. After 10 redox cycles, no significant change in morphology was observed for both carriers, indicating that the reaction conditions were not leading to sintering. The EDS elemental mapping for both the fresh and post redox carriers, depicted in Fig. S6–S9,† confirm no phase segregation.

These characterization results confirm that the $VOPO_4$ can maintain its phase and textural integrity across multiple redox cycles in both the supported and unsupported carriers. However, to understand the transformation of $VOPO_4$ as it reacts with CH_3OH, XRD and XPS analysis was conducted on a VPO-Un carrier that has undergone a 3 hours reduction under CH_3OH at 400 °C.

The XRD analysis of the post 3 hours reduced sample, shown in Fig. 6(a), reveals the formation of the $(VO)_2P_2O_7$ (ICDD – 00-050-0380) and the $VPO_4.H_2O$ (ICDD – 01-088-1244) phase. Thus, the sample is reduced from its +5 oxidation state of V in $VOPO_4$ to +4 and +3 oxidation states. Furthermore, this reduced

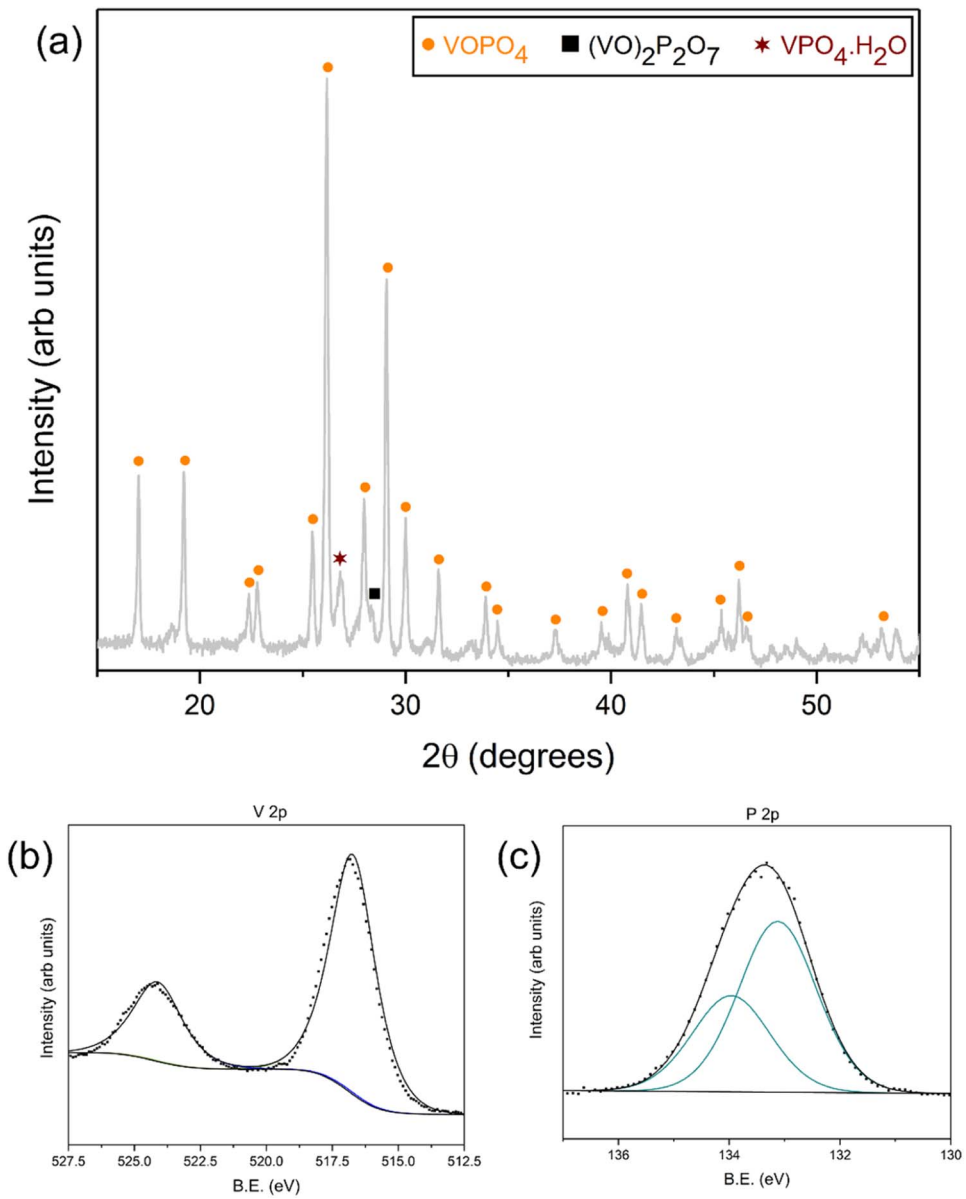

Fig. 6 (a) XRD spectra (b) V 2p XPS spectra and (c) P 2p XPS spectra of VPO-Un after 3 hours CH_3OH reduction.

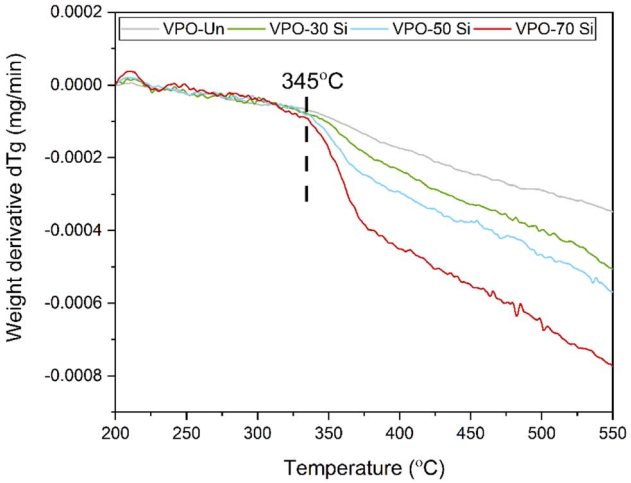

Fig. 7 Temperature programmed reduction of VPO-Un, VPO-30Si, VPO-50Si, and VPO-70Si carriers.

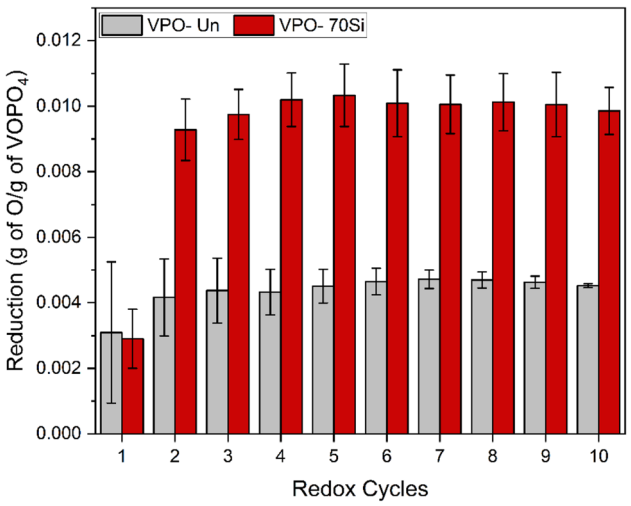

Fig. 8 Oxygen loss of VPO-Un and VPO-70Si carriers across 10 redox cycles.

sample, when exposed to air at 550 °C, regenerates back to the original $VOPO_4$ phase, as depicted in Fig. S10.† Complementary XPS spectra were collected to further confirm the oxidation states. The V 2p spectra, shown in Fig. 6(b), indicate that there is only the V^{4+} state remaining on the surface of the material (516.7 eV and 524.1 eV for V $2p_{3/2}$ and V $2p_{1/2}$, respectively). The P 2p region of the same material is shown in Fig. 6(c), which is the doublet of P $2p_{3/2}$ (133.1 eV) and P $2p_{1/2}$ (134.0 eV). This is a slightly higher binding energy than the previous P 2p spectra and could be due to the formation of a different phase, as indicated in Fig. 6(a).[65–67] The XPS analysis for other elements is provided in ESI (Section S7).†

3.2 Thermogravimetric analysis

Although the solid characterization analysis confirms that SiO_2 does not react with β-$VOPO_4$, TPR experiments were performed to investigate the effect of SiO_2 on carrier reactivity. Unsupported $VOPO_4$, along with SiO_2 supported $VOPO_4$ carriers, were subjected to CH_3OH TPR after 1 redox cycle, as shown in Fig. 7. All the carriers start reacting with CH_3OH around ~345 °C, indicating that the addition of SiO_2 does not seem to alter the intrinsic kinetics of the reaction. However, the magnitude of the peak increases with an increase in SiO_2 concentration. This implies that the addition of SiO_2 as support improves the dispersion of $VOPO_4$, enhancing the reactivity.

To evaluate the reactivity and recyclability of the carriers, 10 continuous redox cycles were performed. The oxygen loss calculated based on TGA weight reduction data for the VPO-Un and VPO-70Si is presented in Fig. 8. For both carriers, the oxygen loss improves after the 1st cycle, which can be attributed to carrier activation, a phenomenon observed in many chemical looping applications.[68–70] An oxygen loss improvement of ~35% and ~220% is observed after the 1st cycle for VPO-Un and VPO-70Si, respectively. From the 2nd cycle, both the carriers maintain their reactivity, which is congruous with the SEM analysis as no sintering was observed, as discussed in Section 3.1.2. However, the oxygen loss for the VPO-70Si carrier is ~115% higher than the VPO-Un carrier. This drastic reactivity improvement can be attributed to the higher dispersion of $VOPO_4$ on the SiO_2 support, confirmed through the TPR study. Furthermore, redox analysis for VPO-30Si and VPO-50Si along with the results presented in Fig. 8 support the conclusion of $VOPO_4$ dispersion on SiO_2 drawn from TPR results and is shown in Fig. S12.† This result establishes the exceptional performance of the SiO_2-supported carrier in terms of reactivity and recyclability over the unsupported carrier.

3.3 Fixed bed analysis

After the assessment of reactivity and recyclability, gaseous product analysis for the CLMO process was carried out in fixed bed mode to gauge the performance at a higher scale of operation. The VPO-Un and VPO-70Si carrier were subjected to

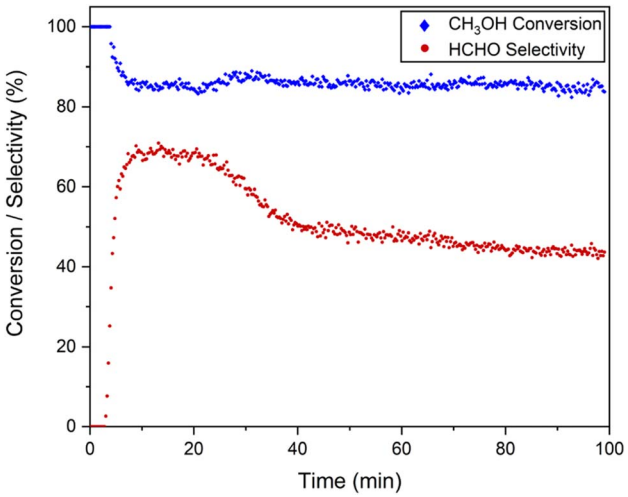

Fig. 9 CH_3OH conversion and HCHO selectivity profile of VPO-70Si in fixed bed.

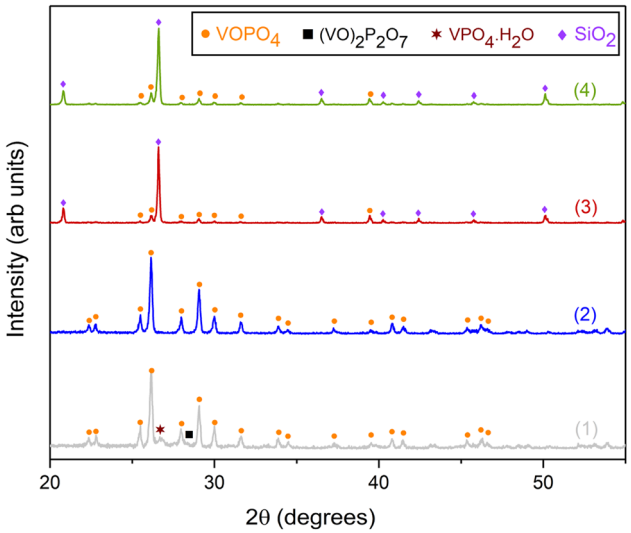

Fig. 10 XRD spectra of VPO-Un (1) post reduction and (2) post regeneration and of VPO-70Si (3) post reduction and (4) post regeneration.

CH_3OH reduction at 400 °C. The trend for CH_3OH conversion and HCHO selectivity for VPO-70Si is presented in Fig. 9, with the concentration profile depicted in Fig. S13.† The analysis for the VPO-Un carrier is shown in Fig. S14.† At 400 °C, a steady CH_3OH conversion of ~85% with average HCHO selectivity of ~45% is achieved for both carriers. The recorded IR spectra of the reactor outlet gas stream at different time intervals during the VPO-70Si reduction is presented in Fig. S15.† The spectra clearly reveal the formation of formaldehyde as the major product. Furthermore, the selectivity towards formaldehyde is reported to be highest among oxygenates apart from CO_2, and CO for the catalytic selective oxidation of methanol over vanadium phosphorous oxide-based catalysts at 400 °C.[13,40] Nevertheless, future studies will investigate whether such products apart from those mentioned are being formed.

As shown in Fig. 10, the XRD spectra of the VPO-Un post CH_3OH reduction at 400 °C reveal the presence of $VPO_4.H_2O$ and $(VO)_2P_2O_7$ phases. The peak for the $VPO_4.H_2O$ phase in the reduced VPO-70Si XRD spectra, also shown in Fig. 10, is masked due to the overlap of the high intensity SiO_2 peak at ~26.8°, and the peak for the $(VO)_2P_2O_7$ is too small to be detected. However, these peaks are clearly visible in the reduced VPO-Un carrier, confirming the formation of oxygen deficient phases. Additionally, the XRD spectra show no impurity phase formation after the CH_3OH reduction and air oxidation steps for both carriers, thereby confirming the carriers' phase stability and validating the recyclability studies performed in the earlier section. A balance on the carbonaceous species of the system revealed a steady carbon deficit, with an average value of ~30%, indicative of carbon deposition in the system. However, as discussed above, no other peak apart from CO, CO_2, CH_3OH, and HCHO is detected in the outlet FTIR spectra (Fig. S15†), leading to the assumption that carbon deposition is occurring.

However, TEM images of the VPO-Un fresh and post fixed bed reduction samples, illustrated in Fig. 11, do not show any evidence of carbon deposition. To confirm whether any carbon deposition was occurring on the carrier, several TGA studies were conducted, wherein the VPO-Un carrier was reduced under CH_3OH (1000 ppm) for extended time periods, as depicted in Fig. S16.† The TGA curves, depicting weight *versus* time, revealed a continuous decrease in weight, indicating loss of lattice oxygen from the carrier. Even after subjecting the carrier to a 12 hours reduction, albeit at a higher gas to solid ratio compared to fixed-bed, no increase in weight, typically associated with carbon deposition, was observed. The carbon deposition in the fixed bed could be attributed to the higher partial pressures of reactant and product gases compared to TGA on the sites provided by the ceramic reactor wall material. However, if any other products apart from CO, CO_2 and HCHO are being formed, with the intensity of their spectra below the detection limit of FTIR, such products can justify the observed carbon error. As mentioned above, the aim of this study is to establish a proof of concept for formaldehyde production from methanol using the chemical looping route. The future work will involve gaining insights into the carbon balance through comprehensive gas analysis and suggest appropriate changes to the reactor setup or configuration if it is found that carbon deposition is due to reactor effects. Further optimization of the

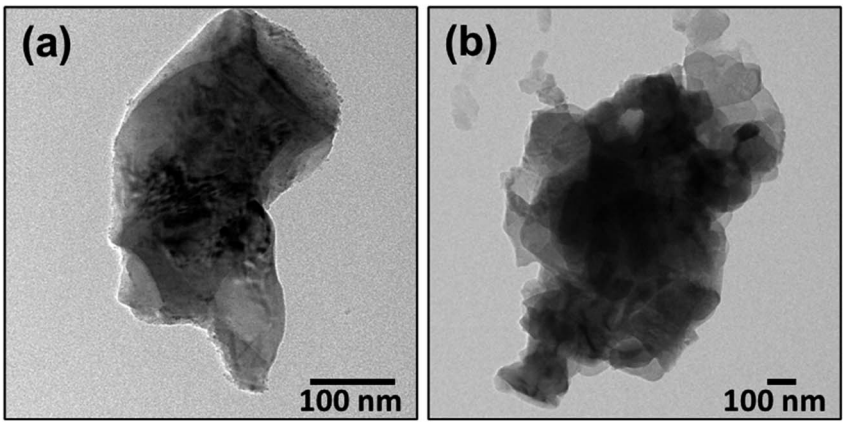

Fig. 11 TEM images of VPO-Un (a) before and (b) after fixed bed reduction.

carrier through dopant modification will also be carried out to improve the product yield.

4. Conclusions

A first of its kind chemical looping scheme for HCHO production from CH_3OH was successfully established in this work, which renders safer operation by avoiding the contact of CH_3OH and O_2. The selective oxidation property of vanadium phosphorous oxides (VPO), in conjunction with its lattice oxygen, was leveraged to develop high-performance and robust oxygen carriers by dispersing the most oxidized phase of VPO ($VOPO_4$) on SiO_2 support. It was found that the rate of reduction of the carriers depends on the concentration of SiO_2 in the carrier. The temperature programmed analysis revealed that although the addition of SiO_2 support does not seem to intrinsically affect the reaction mechanism, it improves the dispersion of $VOPO_4$, the active component. Furthermore, redox analysis confirmed the stability of the carriers and validated that the addition of support improves reactivity as the VPO-70Si carrier showcased ~115% higher oxygen loss rate compared to the unsupported carrier. XPS results suggested the presence of oxygen vacancies on the surface of the carrier as the ratio of V^{5+}/V^{4+} decreases after 10 redox cycles. However, no change in reactivity was observed from the 2nd to the 10th cycle, and further research can focus on investigating the evolution and effect of these vacancies. Fixed bed analysis exhibited stable CH_3OH conversion of ~85% with selectivity towards HCHO of ~45% for the VPO-70Si carrier. Carbon deposition was observed in the fixed bed study, however, understanding its formation will be part of a future study. The design concept of a carrier targeted towards a specific reaction, exemplified in this work for selective oxidation for CH_3OH through VPO carriers, can be extended to other applications as well. Furthermore, as this work is among the very few in the field of chemical looping selective oxidation apart from H_2 and syngas generation, it can help to advance research in this field.

Conflicts of interest

The authors declare that they have no known competing financial interests or personal relationships that could have appeared to influence the work reported in this paper.

Note added after first publication

This article replaces the version published on 24 February 2024, which contained a typographical error in eqn (3) that has since been corrected.

Acknowledgements

The authors wish to thank the funds of the C. John Easton Professorship in Engineering in the Department of Chemical and Biomolecular Engineering at The Ohio State University that support this study. The service provided by the Center for Electron Microscopy and Analysis (CEMAS) at The Ohio State University and Dr Sameera Perera at the Lumigen Instrument Center at Wayne State University is greatly appreciated. Helpful discussions with Dr Vedant Shah are acknowledged by the authors.

References

1 J. Thrane, U. V. Mentzel, M. Thorhauge, M. Høj and A. D. Jensen, A Review and Experimental Revisit of Alternative Catalysts for Selective Oxidation of Methanol to Formaldehyde, *Catalysts*, 2021, **11**(11), 1329.
2 A. P. V. Soares, M. F. Portela and A. Kiennemann, Methanol Selective Oxidation to Formaldehyde over Iron-molybdate Catalysts, *Catal. Rev.*, 2005, **47**(1), 125–174.
3 *Sharing insights elevates their impact*, S&P Global, **https://www.spglobal.com/commodityinsights/en/ci/products/formaldehyde-chemical-economics-handbook.html**, accessed 2023-06-11.
4 P. Solt, J. Konnerth, W. Gindl-Altmutter, W. Kantner, J. Moser, R. Mitter and H. W. van Herwijnen, Technological Performance of Formaldehyde-Free Adhesive Alternatives for Particleboard Industry, *Int. J. Adhes. Adhes.*, 2019, **94**, 99–131.
5 L. Zhang, *Formaldehyde: Exposure, Toxicity and Health Effects*, Royal Society of Chemistry, 2018, vol. 37.
6 M. I. Malik, N. Abatzoglou and I. E. Achouri, Methanol to Formaldehyde: An Overview of Surface Studies and Performance of an Iron Molybdate Catalyst, *Catalysts*, 2021, **11**(8), 893.
7 S. Deshmukh, M. van Sint Annaland and J. A. M. Kuipers, Kinetics of the Partial Oxidation of Methanol over a Fe-Mo Catalyst, *Appl. Catal., A*, 2005, **289**(2), 240–255.
8 L. E. Heim, H. Konnerth and M. H. Prechtl, Future Perspectives for Formaldehyde: Pathways for Reductive Synthesis and Energy Storage, *Green Chem.*, 2017, **19**(10), 2347–2355.
9 L. Zhang, Introduction to Formaldehyde, *Issues in Toxicology*, Royal Society of Chemistry, London, UK, 2018, pp. 1–19.
10 A. M. Bahmanpour, A. Hoadley and A. Tanksale, Critical Review and Exergy Analysis of Formaldehyde Production Processes, *Rev. Chem. Eng.*, 2014, **30**(6), 583–604.
11 A. W. Franz, H. Kronemayer, D. Pfeiffer, R. D. Pilz, G. Reuss, W. Disteldorf, A. O. Gamer and A. Hilt, *Formaldehyde, Ullmann's Encyclopedia of Industrial Chemistry*, Wiley-VCH Verlag GmbH & Co. KGaA Weinbeim, Germany, 2016.
12 H. R. Gerberich and G. C. Seaman, Hoechst-Celanese Corporation Formaldehyde, *Kirk-Othmer Encyclopedia of Chemical Technology*, John Wiley & Sons, Inc., Hoboken, NJ, USA, 2013, pp. 24–26.
13 G. C. Behera, K. Parida, N. F. Dummer, G. Whiting, N. Sahu, A. F. Carley, M. Conte, G. J. Hutchings and J. K. Bartley, Tungstate Promoted Vanadium Phosphate Catalysts for the Gas Phase Oxidation of Methanol to Formaldehyde, *Catal. Sci. Technol.*, 2013, **3**(6), 1558–1564.
14 X. Liu, L. Kong, S. Xu, C. Liu and F. Ma, Modified Iron-Molybdate Catalysts with Various Metal Oxides by

a Mechanochemical Method: Enhanced Formaldehyde Yield in Methanol Partial Oxidation, *Front. Chem. Sci. Eng.*, 2021, **15**, 1099–1110.

15 S. H. Taylor, Reflections on Catalytic Selective Oxidation: Opportunities and Challenges, *Catalysts*, 2017, **7**(1), 34.

16 G. J. Millar and M. Collins, Industrial Production of Formaldehyde Using Polycrystalline Silver Catalyst, *Ind. Eng. Chem. Res.*, 2017, **56**(33), 9247–9265.

17 C. Brookes, P. P. Wells, N. Dimitratos, W. Jones, E. K. Gibson, D. J. Morgan, G. Cibin, C. Nicklin, D. Mora-Fonz and D. O. Scanlon, The Nature of the Molybdenum Surface in Iron Molybdate. The Active Phase in Selective Methanol Oxidation, *J. Phys. Chem. C*, 2014, **118**(45), 26155–26161.

18 A. Gaur, M. Stehle, K. V. Raun, J. Thrane, A. D. Jensen, J.-D. Grunwaldt and M. Høj, Structural Dynamics of an Iron Molybdate Catalyst under Redox Cycling Conditions Studied with in Situ Multi Edge XAS and XRD, *Phys. Chem. Chem. Phys.*, 2020, **22**(20), 11713–11723.

19 N. V. Nikolenko, A. O. Kosynyuk, Y. V. Kalashnikov and E. A. Cheremis, The Calculation of the Thermodynamic Equilibrium in Fe^{3+}/MoO 4 2−/H+(OH−)/H 2 O System and Determination of Reasonable Conditions for Iron Molybdate Deposition, *Russ. J. Appl. Chem.*, 2012, **85**, 1814–1819.

20 N. V. Nikolenko, I. V. Kozhevnikov, A. O. Kostyniuk, H. Bayahia and Y. V. Kalashnykov, Preparation of Iron Molybdate Catalysts for Methanol to Formaldehyde Oxidation Based on Ammonium Molybdoferrate (II) Precursor, *J. Saudi Chem. Soc.*, 2018, **22**(3), 372–379.

21 D. S. Baser, S. G. Nadgouda, A. S. Joshi and L.-S. Fan, 110th Anniversary: Indirect Partial Oxidation of Methane Using a Counter-Current Moving-Bed Chemical Looping Configuration for Enhanced Syngas Production, *Ind. Eng. Chem. Res.*, 2019, **58**(36), 16407–16416, DOI: **10.1021/acs.iecr.9b02520**.

22 R. Joshi, Y. Pottimurthy, V. Shah, P. Mohapatra, S. Kumar, O. Jones, M. Beard, I. Harry, A. Hornbuckle, M. Kathe and L.-S. Fan, Coal-Direct Chemical Looping Process with In Situ Sulfur Capture for Energy Generation Using Ca–Cu Oxygen Carriers, *Ind. Eng. Chem. Res.*, 2021, **60**(30), 11231–11240, DOI: **10.1021/acs.iecr.1c01814**.

23 A. S. Joshi, K. V. Jangam, Z. Mohammad and L.-S. Fan, Novel Sulfur Looping Scheme to Convert H2S to H2 Using Ni3S2 Supported over ZrO2: Thermodynamic, Kinetic, and Comparative System Analyses, *Fuel Process. Technol.*, 2022, **237**, 107443, DOI: **10.1016/j.fuproc.2022.107443**.

24 D. Wang, A. Joshi and L.-S. Fan, Chemical Looping Technology – a Manifestation of a Novel Fluidization and Fluid-Particle System for CO2 Capture and Clean Energy Conversions, *Powder Technol.*, 2022, **409**, 117814, DOI: **10.1016/j.powtec.2022.117814**.

25 A. Joshi, R. K. Joshi, E. Falascino, T. A. Jawdekar, S. G. Shinde, D. Baser, S. Patil and L.-S. Fan, Thermodynamic Evaluation of the Cross-Current Moving-Bed Chemical Looping Configuration for Efficient Conversion of Biomass to Syngas, *Energy Fuels*, 2023, **37**(21), 16744–16756, DOI: **10.1021/acs.energyfuels.3c02934**.

26 C. Park, R. K. Joshi, E. Falascino, Y. Pottimurthy, D. Xu, D. Wang, A. Sunny, S. Hwang, A. S. Joshi, P. Mohapatra, S. Kumar, Q. Zhang, Q. Meng, V. Shah, A. Tong and L.-S. Fan, Biomass Gasification: Sub-Pilot Operation of >600 h with Extensive Tar Cracking Property and High Purity Syngas Production at H2:CO Ratio ∼2 Using Moving Bed Redox Looping Technology, *Fuel Process. Technol.*, 2023, **252**, 107966, DOI: **10.1016/j.fuproc.2023.107966**.

27 A. A. Sunny, Q. Meng, S. Kumar, R. Joshi and L.-S. Fan, Nanoscaled Oxygen Carrier-Driven Chemical Looping for Carbon Neutrality: Opportunities and Challenges, *Acc. Chem. Res.*, 2023, 3c00517, DOI: **10.1021/acs.accounts.3c00517**.

28 D. Zeng, Y. Qiu, S. Peng, C. Chen, J. Zeng, S. Zhang and R. Xiao, Enhanced Hydrogen Production Performance through Controllable Redox Exsolution within $CoFeAlO_x$ Spinel Oxygen Carrier Materials, *J. Mater. Chem. A*, 2018, **6**(24), 11306–11316, DOI: **10.1039/C8TA02477D**.

29 Z. Sun, X. Wu, C. K. Russell, M. D. Dyar, E. C. Sklute, S. Toan, M. Fan, L. Duan and W. Xiang, Synergistic Enhancement of Chemical Looping-Based CO_2 Splitting with Biomass Cascade Utilization Using Cyclic Stabilized $Ca_2Fe_2O_5$ Aerogel, *J. Mater. Chem. A*, 2019, **7**(3), 1216–1226, DOI: **10.1039/C8TA10277E**.

30 S. Feng, W. Gao, Q. Wang, Y. Guan, H. Yan, H. Wu, H. Cao, J. Guo and P. Chen, A Multi-Functional Composite Nitrogen Carrier for Ammonia Production *via* a Chemical Looping Route, *J. Mater. Chem. A*, 2021, **9**(2), 1039–1047, DOI: **10.1039/D0TA10519H**.

31 A. Joshi, V. Shah, P. Mohapatra, S. Kumar, R. K. Joshi, M. Kathe, L. Qin, A. Tong and L.-S. Fan, Chemical Looping-A Perspective on the next-Gen Technology for Efficient Fossil Fuel Utilization, *Adv. Appl. Energy*, 2021, **3**, 100044, DOI: **10.1016/j.adapen.2021.100044**.

32 D. Zeng, Y. Qiu, M. Li, L. Ma, D. Cui, S. Zhang and R. Xiao, Spatially Controlled Oxygen Storage Materials Improved the Syngas Selectivity on Chemical Looping Methane Conversion, *Appl. Catal., B*, 2021, **281**, 119472.

33 A. Joshi, P. Mohapatra, R. Joshi, S. Kumar, A. Sunny, Z. Cheng, L. Qin and L.-S. Fan, Advances in Chemical Looping Combustion Technology, in *Combustion Chemistry and the Carbon Neutral Future*, Elsevier, 2023, pp. 383–416.

34 S. Liang, Y. Liao, W. Li, C. Li and X. Ma, Enhanced Stability of Iron-Nickel Oxygen Carriers in Biomass Chemical Looping Gasification by Core-Shell Structure, *Chem. Eng. J.*, 2023, **451**, 138964.

35 G. Luongo, A. H. Bork, P. M. Abdala, Y.-H. Wu, E. Kountoupi, F. Donat and C. R. Müller, Activation in the Rate of Oxygen Release of Sr 0.8 Ca 0.2 $FeO_3-\delta$ through Removal of Secondary Surface Species with Thermal Treatment in a CO_2 -Free Atmosphere, *J. Mater. Chem. A*, 2023, **11**(12), 6530–6542, DOI: **10.1039/D2TA09102J**.

36 B. Jiang, L. Li, Q. Zhang, J. Ma, H. Zhang, K. Yu, Z. Bian, X. Zhang, X. Ma and D. Tang, Iron–Oxygen Covalency in Perovskites to Dominate Syngas Yield in Chemical Looping

Partial Oxidation, *J. Mater. Chem. A*, 2021, **9**(22), 13008–13018, DOI: 10.1039/D1TA02103F.

37 N. V. R. A. Dharanipragada, L. C. Buelens, H. Poelman, E. De Grave, V. V. Galvita and G. B. Marin, Mg–Fe–Al–O for Advanced CO_2 to CO Conversion: Carbon Monoxide Yield vs. Oxygen Storage Capacity, *J. Mater. Chem. A*, 2015, **3**(31), 16251–16262, DOI: 10.1039/C5TA02289D.

38 G. Mishra, G. C. Behera, S. K. Singh and K. Parida, Facile Synthesis and Synergetic Interaction of VPO/β-SiC Composites toward Solvent-Free Oxidation of Methanol to Formaldehyde, *ACS Omega*, 2020, **5**(36), 22808–22815, DOI: 10.1021/acsomega.0c01921.

39 F. Blanco-Bonilla, R. Estevez, F. J. López-Tenllado, D. Luna and F. M. Bautista, Selective Oxidation of Methanol to Green Oxygenates on Vanadium-Aluminum Phosphate Based Catalysts, *Catal. Today*, 2024, **430**, 114517, DOI: 10.1016/j.cattod.2024.114517.

40 G. C. Behera and K. Parida, Selective Gas Phase Oxidation of Methanol to Formaldehyde over Aluminum Promoted Vanadium Phosphate, *Chem. Eng. J.*, 2012, **180**, 270–276.

41 M. Faizan, R. Zhang and R. Liu, Vanadium Phosphorus Oxide Catalyst: Progress, Development and Applications, *J. Ind. Eng. Chem.*, 2022, **110**, 27–67.

42 S. Kumar, P. Mohapatra, R. K. Joshi, M. Warburton and L.-S. Fan, Synergistic Chemical Looping Process Coupling Natural Gas Conversion and NO*x* Purification, *Energy Fuels*, 2023, **37**(10), 7268–7279.

43 Y. Zheng, K. Li, H. Wang, D. Tian, Y. Wang, X. Zhu, Y. Wei, M. Zheng and Y. Luo, Designed Oxygen Carriers from Macroporous $LaFeO_3$ Supported CeO_2 for Chemical-Looping Reforming of Methane, *Appl. Catal., B*, 2017, **202**, 51–63.

44 R. Liu, X. Zhang, T. Liu, X. Yao, Z. Zhao, C. Pei and J. Gong, Dynamic Oxygen Migration and Reaction over Ceria-Supported Nickel Oxides in Chemical Looping Partial Oxidation of Methane, *Appl. Catal., B*, 2023, **328**, 122478.

45 S. Daneshmand-Jahromi, M. H. Sedghkerdar and N. Mahinpey, Synthesis, Characterization, and Kinetic Study of Nanostructured Copper-Based Oxygen Carrier Supported on Silica and Zirconia Aerogels in the Cyclic Chemical Looping Combustion Process, *Chem. Eng. J.*, 2022, **448**, 137756.

46 D. Zeng, F. Kang, Y. Qiu, D. Cui, M. Li, L. Ma, S. Zhang and R. Xiao, Iron Oxides with Gadolinium-Doped Cerium Oxides as Active Supports for Chemical Looping Hydrogen Production, *Chem. Eng. J.*, 2020, **396**, 125153.

47 H. Zhao, C. Zuo, D. Yang, C. Li and S. Zhang, Effects of Support for Vanadium Phosphorus Oxide Catalysts on Vapor-Phase Aldol Condensation of Methyl Acetate with Formaldehyde, *Ind. Eng. Chem. Res.*, 2016, **55**(50), 12693–12702.

48 H. Song, K. Shah, E. Doroodchi and B. Moghtaderi, Development of a Cu–Mg-Based Oxygen Carrier with SiO2 as a Support for Chemical Looping Air Separation, *Energy Fuels*, 2014, **28**(1), 163–172, DOI: 10.1021/ef401485p.

49 V. Fleischer, U. Simon, S. Parishan, M. G. Colmenares, O. Görke, A. Gurlo, W. Riedel, L. Thum, J. Schmidt, T. Risse, K.-P. Dinse and R. Schomäcker, Investigation of the Role of the Na_2WO_4/Mn/SiO_2 Catalyst Composition in the Oxidative Coupling of Methane by Chemical Looping Experiments, *J. Catal.*, 2018, **360**, 102–117, DOI: 10.1016/j.jcat.2018.01.022.

50 Z. Cheng, A. Joshi and L.-S. Fan, Chemical Looping Clean Energy Technology Toward a Low-Carbon Future, *Engineering*, 2023, S2095809923003788, DOI: 10.1016/j.eng.2023.08.008.

51 B. Chen and E. J. Munson, Investigation of the Mechanism of N-Butane Oxidation on Vanadium Phosphorus Oxide Catalysts: Evidence from Isotopic Labeling Studies, *J. Am. Chem. Soc.*, 2002, **124**(8), 1638–1652.

52 S. Lowell and J. E. Shields, Adsorption Isotherms, in *Powder Surface Area and Porosity*, ed. S. Lowell and J. E. Shields, Springer Netherlands, Dordrecht, 1984, pp. 11–13, DOI: 10.1007/978-94-009-5562-2_3.

53 M. E. Lashier and G. L. Schrader, Reactive Lattice Oxygen Sites for C4 Hydrocarbon Selective Oxidation over β-VOPO4, *J. Catal.*, 1991, **128**(1), 113–125.

54 H. Numata and T. Ono, Redox Features of β-$VOPO_4$ Catalyst Using 18O Tracer and Laser Raman Spectroscopy, *J. Mol. Catal. A: Chem.*, 1998, **130**(3), 261–269, DOI: 10.1016/S1381-1169(97)00217-3.

55 Y. Ni and G. He, Stable Cycling of β-$VOPO_4$/$NaVOPO_4$ Cathodes for Sodium-Ion Batteries, *Electrochim. Acta*, 2018, **292**, 47–54.

56 A. Tang, Z. Liang, H. Chen, G. Xu and H. Song, V_2O_3–Li_3PO_4 Composite: A New Type of Cathodic Active Material for Li-Ion Batteries, *Adv. Mater. Interfaces*, 2022, **9**(13), 2101955, DOI: 10.1002/admi.202101955.

57 L. Ruiz-Rodríguez, A. de Arriba, A. Vidal-Moya, T. Blasco, E. Rodríguez-Castellón and J. M. López Nieto, The Role of Promoters on the Catalytic Performance of MxV2O5 Bronzes for the Selective Partial Oxidation of H2S, *Appl. Catal., A*, 2022, **647**, 118900, DOI: 10.1016/j.apcata.2022.118900.

58 M. Nadolska, M. Szkoda, K. Trzciński, P. Niedziałkowski, J. Ryl, A. Mielewczyk-Gryń, K. Górnicka and M. Prześniak-Welenc, Insight into Potassium Vanadates as Visible-Light-Driven Photocatalysts: Synthesis of V(IV)-Rich Nano/Microstructures for the Photodegradation of Methylene Blue, *Inorg. Chem.*, 2022, **61**(25), 9433–9444, DOI: 10.1021/acs.inorgchem.2c00136.

59 Y. Zhang, R. Zhang, J. Dong, Y. Wu, C. Luo, H. Zhang, S. Zhu and R. Liu, The Critical Role of Steam during Activation Process on the Catalytic Performance of VPO for N-Butane Selective Oxidation to Maleic Anhydride, *J. Catal.*, 2022, **416**, 157–169, DOI: 10.1016/j.jcat.2022.11.004.

60 K. Zhao, L. Yang, L. Qian, Y. Zhang, J. Hou, P. Christie, W. Liu and P. Qi, Elimination of Chromium(VI) and Vanadium(V) from Waters by Carboxymethylcellulose-Stabilized Amorphous Nanoscale Zero-Valent Iron, *Water, Air, Soil Pollut.*, 2022, **233**(12), 499, DOI: 10.1007/s11270-022-05899-w.

61 L. Liu, T. Yuan, Z. Li, K. Chen and W. Huang, Hydrogenated V_2O_5 with Fast Zn-Ion Migration Kinetics as High-

Performance Cathode Material for Aqueous Zinc-Ion Batteries, *Electrochim. Acta*, 2023, **439**, 141717, DOI: 10.1016/j.electacta.2022.141717.

62 J. Wen, X. Hou, M. Yao, J. Chen, M. Tian, E. Feng, G. Huang and S. Xu, Tuning of Vanadium Valence for Value-Added Recycling and Utilization of Vanadium from Spent Selective Catalytic Reduction Catalysts, *J. Cleaner Prod.*, 2023, **390**, 136151, DOI: 10.1016/j.jclepro.2023.136151.

63 X. Yang and J. Zou, Facile Fabrication of VO_2 Composite Film with Enhanced Significantly Solar Modulation Performance by Adjusting Viscosity of VO_2/PU Dispersion, *J. Alloys Compd.*, 2023, **940**, 168868, DOI: 10.1016/j.jallcom.2023.168868.

64 G. Silversmit, D. Depla, H. Poelman, G. B. Marin and R. De Gryse, Determination of the V2p XPS Binding Energies for Different Vanadium Oxidation States (V5+ to V0+), *J. Electron Spectrosc. Relat. Phenom.*, 2004, **135**(2), 167–175, DOI: 10.1016/j.elspec.2004.03.004.

65 M. J. Valero-Romero, A. Cabrera-Molina, M. O. Guerrero-Pérez, J. Rodríguez-Mirasol and T. Cordero, Carbon Materials as Template for the Preparation of Mixed Oxides with Controlled Morphology and Porous Structure, *Catal. Today*, 2014, **227**, 233–241, DOI: 10.1016/j.cattod.2013.10.093.

66 M. O. Guerrero-Pérez, M. J. Valero-Romero, S. Hernández, J. M. L. Nieto, J. Rodríguez-Mirasol and T. Cordero, Lignocellulosic-Derived Mesoporous Materials: An Answer to Manufacturing Non-Expensive Catalysts Useful for the Biorefinery Processes, *Catal. Today*, 2012, **195**(1), 155–161, DOI: 10.1016/j.cattod.2012.03.068.

67 J. M. Rosas, R. Ruiz-Rosas, J. Rodríguez-Mirasol and T. Cordero, Kinetic Study of the Oxidation Resistance of Phosphorus-Containing Activated Carbons, *Carbon*, 2012, **50**(4), 1523–1537, DOI: 10.1016/j.carbon.2011.11.030.

68 V. Shah, Z. Cheng, D. S. Baser, J. A. Fan and L.-S. Fan, Highly Selective Production of Syngas from Chemical Looping Reforming of Methane with CO_2 Utilization on MgO-Supported Calcium Ferrite Redox Materials, *Appl. Energy*, 2021, **282**, 116111, DOI: 10.1016/j.apenergy.2020.116111.

69 K. V. Jangam, A. S. Joshi, Y.-Y. Chen, S. Mahalingam, A. A. Sunny and L.-S. Fan, Synergistic Decomposition of H_2S into H_2 by Ni3S2 over ZrO_2 Support via a Sulfur Looping Scheme with CO_2 Enabled Carrier Regeneration, *Chem. Eng. J.*, 2021, **426**, 131815, DOI: 10.1016/j.cej.2021.131815.

70 K. Jangam, Y.-Y. Chen, L. Qin and L.-S. Fan, Mo-Doped FeS Mediated H_2 Production from H_2S via an In Situ Cyclic Sulfur Looping Scheme, *ACS Sustainable Chem. Eng.*, 2021, **9**(33), 11204–11211, DOI: 10.1021/acssuschemeng.1c03410.